

# Ultrastrong magnetic light-matter interaction with cavity mode engineering

Hyeonrak Choi\* and Dirk Englund†

Research Laboratory of Electronics, Massachusetts Institute of Technology, Cambridge, Massachusetts 02139, USA

(Dated: August 31, 2021)

Magnetic interaction between photons and dipoles is essential in electronics, sensing, spectroscopy, and quantum computing. However, its weak strength often requires resonators to confine and store the photons. Here, we present mode engineering techniques to create resonators with ultrasmall mode volume and ultrahigh quality factor. In particular, we show that it is possible to achieve an arbitrarily small mode volume only limited by materials or fabrication with minimal  $Q$  degradation. We compare mode-engineered cavities in a trade-off space and show that the magnetic interaction can be strengthened more than  $10^{16}$  times compared to free space. These methods enable new applications from high-cooperativity microwave-spin coupling in quantum computing or compact electron paramagnetic resonance (EPR) sensors to fundamental science such as dark matter searches.

The magnetic light-matter interaction has a wide range of applications including quantum computing [1] and sensing [2], nuclear magnetic resonance (NMR) [3], microwave (MW) active devices [4], and MW amplification by stimulated emission of radiation (maser) [5]. However, the magnetic interaction is intrinsically weak compared with the electrical counterpart [6]. It is possible to increase the coupling by designing resonators with a strong magnetic field and long interaction time – i.e., a small magnetic mode volume ( $V_B$ ) and a high quality factor ( $Q$ ). This is especially important in quantum applications requiring strong interaction between a single photon and magnetic dipoles. Here, we present and compare three mode engineering techniques to reduce the mode volume: longitudinal mode squeezing with  $\text{TM}_{mn0}$  modes, current engineering, and magnetic field expulsion. We show that all three methods enable arbitrarily small  $V_B$  only limited by the electromagnetic (EM) penetration depth, typically on the order of tens of nanometers for superconductors. The reduction of  $V_B$  accompanies a reduction of  $Q$ , but  $Q/V_B$ , a figure of merit for light-matter interaction, can increase more than five orders of magnitude with plausible fabrication assumptions. Ultrastrong magnetic interaction by mode engineering enables new applications including microwave to optical transduction, low-noise masers, magnetic strong coupling of spin qubits or superconducting qubits, and cavity magnonics.

A magnetic dipole interacts with EM fields through the interaction Hamiltonian  $H_{\text{int}} = -\vec{m} \cdot \vec{B}$ , where  $\vec{m}$  is the magnetic transition dipole moment and  $\vec{B}$  is the magnetic flux density. (For simplicity, we will refer to  $\vec{B}$  as the magnetic field.) For cavity photons, the single photon magnetic field  $B_s$  is,

$$B_s(\vec{r}) = \sqrt{\frac{hf}{2V_B(\vec{r})/\mu}}, \quad (1)$$

where  $hf$  is the photon energy,  $\mu$  is the permeability of the cavity filling, and  $V_B$  is the effective magnetic mode

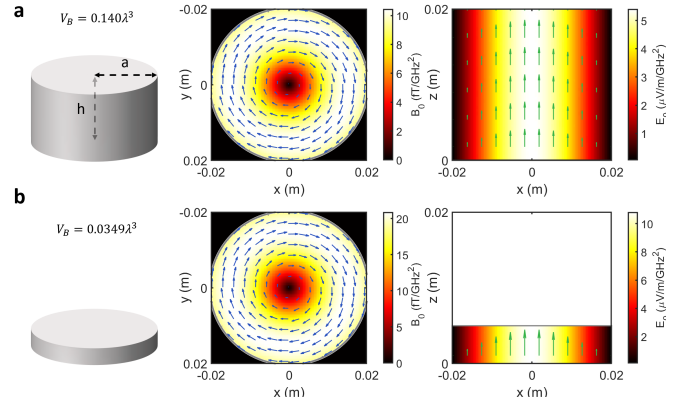


FIG. 1. **Longitudinal squeezing of the  $\text{TM}_{010}$  mode in a cylindrical cavity.** The radii of the cavities are  $a = 2$  cm, and the heights are **a**,  $h = 2$  cm and **b**, 5 mm. Middle panel: magnetic field of  $\text{TM}_{010}$  mode in  $xy$ -plane. The field is independent of  $z$ . Lengths of the arrows are proportional to the field strength. Right Panel: electric field of  $\text{TM}_{010}$  mode in  $xz$ -plane. The mode is azimuthally symmetric. Resonant frequencies of cavities are the same,  $f = 5.74$  GHz. The magnetic and electric fields are out of phase.

volume of a cavity:

$$V_B(\vec{r}_e) = \frac{\int dV |\vec{B}(\vec{r})|^2 / \mu(\vec{r})}{|\vec{B}(\vec{r}_e)|^2 / \mu(\vec{r}_e)}, \quad (2)$$

where  $\vec{r}_e$  is the position vector of a dipole and chosen for maximum  $|\vec{B}(\vec{r}_e)|$ . On the other hand, cavity photons have a finite lifetime proportional to the quality factor  $Q$ , i.e.  $\tau = Q/2\pi f$ . Thus, a small  $V_B$  as well as high  $Q$  is desirable for light-matter applications.

There have been extensive studies on superconducting qubit [7, 8] and solid-state spin qubit technologies [9–11] on resonators based on coplanar waveguide (CPW) geometries. In CPW resonators, two or more electrically isolated conductors support transverse electromagnetic (TEM) modes with zero cut-off frequency [4]. The transversal Laplace equation allows two conductors to be proximate for a small mode volume. However, the dielectric loss of substrates limits the  $Q$ -factors below one mil-

lion, presenting a critical problem in applications requiring a long photon lifetime [12]. On the other hand, recent progress in 3D transmon [13] based on hollow metallic cavities achieved high  $Q$  over a million [14]. However, their magnetic mode volume is too large to strongly couple photons with qubits because they can support only transverse electric (TE) and transverse magnetic (TM) modes.

Here, we study three approaches of mode engineering of metallic hollow cavities for strong magnetic light-matter interaction. (i) We first study the longitudinally squeezed  $\text{TM}_{mn0}$  mode. (ii) Because the mode volume is inversely proportional to the magnetic field at one point ( $\vec{B}(\vec{r}_e)$ ), we locally increase the magnetic field using current engineering. The framework integrates and derives previously proposed cavity designs such as split mode, loop-gap, and reentrant cavities [15–19]. In addition, our mode engineering enables further reduction of the mode volume through current crowding. (iii) Lastly, motivated by the Meissner effect, we propose a field enhancement method by field expulsion. We compare the cavity designs in terms of  $V_B$  and  $Q$ . In all three methods, we find superconductors have two advantages over the normal conductors: their low MW losses and smaller penetration depth, even at very low frequencies.

### **$\text{TM}_{mn0}$ mode and longitudinal squeezing**

Consider the EM field of the  $\text{TM}_{mnp}$  modes in the cylindrical cavity (Fig. 1) of radius  $a$  and height  $h$ ;

$$E_z = E_0 \cdot J_m(k_c r) \cdot \cos(m\phi) \cdot \cos\left(\frac{\pi p z}{h}\right) \cdot e^{i\omega_{mnp} t} \quad (3)$$

$$B_\phi = E_0 \cdot \frac{i}{\omega} k_c \cdot J'_m(k_c r) \cdot \cos(m\phi) \cdot \cos\left(\frac{\pi p z}{h}\right) \cdot e^{i\omega_{mnp} t},$$

where  $k_c$  is the cut-off wavevector of the base circular waveguide,  $J_m(r)$  the Bessel function of the first kind with the order  $m$ ,  $\omega_{mnp} = c\sqrt{(j_{mn}/a)^2 + (p\pi/h)^2}$ , and  $j_{mn}$  the  $n^{\text{th}}$  zero of  $J_m(r)$ .  $m$ ,  $n$ , and  $p$  represent the azimuthal, radial, and longitudinal wavenumbers.

Cylindrical cavities support  $\text{TM}_{mn0}$  modes where the field is longitudinally uniform. We specifically focus on the lowest order mode,  $\text{TM}_{010}$ ;

$$\begin{aligned} \vec{E}(\vec{r}) &= \hat{z} E_0 \cdot J_0(j_{01} r/a) \cdot e^{i\omega_{010} t} \\ \vec{B}(\vec{r}) &= \hat{\phi} E_0 \cdot \frac{i}{\omega} \frac{j_{01}}{a} \cdot J'_0(j_{01} r/a) \cdot e^{i\omega_{010} t}, \end{aligned} \quad (4)$$

and  $\omega_{010} = c \cdot (j_{01}/a)$ . The resonant frequency is independent of  $h$ , and the cavity can be longitudinally squeezed.

Figure 1a shows the magnetic field (middle) and the electric field (right) of the  $\text{TM}_{010}$  mode of the cylindrical cavity with the radius and height of 0.02 m. We used the finite element method (FEM) with a commercial software (COMSOL). (See Methods for the simulation details). We plot the single-photon magnetic field normalized by frequency square,  $B_0 = B_s/f^2$ . The scale invariance of

Maxwell's equations implies that any cavity mode may be scaled with the wavelength. Thus,  $V_B$  of the same mode is proportional to the wavelength cubed. Equation (1) shows that  $B_s$  is proportional to  $f^2$ , and  $B_0$  serves as a frequency independent metric determined by structural design.

Figure 1b shows the mode of the squeezed cavity ( $h = 0.005$  m). The cavities in fig. 1a and b have the same resonance frequency  $f = 5.74$  GHz. Squeezing from  $h = 0.02$  m to  $h = 0.005$  m does not change the mode field profile in the  $xy$ -plane (independent of  $z$ ), but decreases the volume four times, from  $0.140\lambda^3$  to  $0.0349\lambda^3$  where  $\lambda$  is the vacuum wavelength at resonance. The four-fold increased energy density for fixed energy results in a twice stronger magnetic field. We emphasize that  $\text{TM}_{010}$ -like mode generally exists in any metallic hollow cavities.

$\text{TM}_{010}$  mode volume of a cylindrical cavity is (see Methods),

$$\begin{aligned} V_B &= \frac{0.135}{2\pi} \cdot \frac{j_{01}^2}{|J'_{0,\max}|^2} \cdot h \cdot \lambda^2 \\ &\approx 0.366 \cdot \frac{h}{\lambda} \cdot \lambda^3, \end{aligned} \quad (5)$$

where  $|J'_{0,\max}| \approx 0.582$  is the maximum absolute value of the derivative of the Bessel function. Equation (5) shows that  $V_B$  can be much smaller than  $\lambda^3$  for  $h \ll \lambda$ . For infinitesimally short cavity,  $h \rightarrow 2\delta$ , and  $V_B \rightarrow 0.73\delta\lambda^2$  where  $\delta$  is the penetration depth of the metal.

This contrasts with the usual intuition that the mode volume is diffraction-limited ( $V_B \gtrsim \lambda^3$ ). The EM boundary condition allows perpendicular electric (parallel magnetic) field to be discontinuous with the surface charge (current) on conductors. Because we are not confining EM fields by diffraction, the diffraction limit does not apply. Note that the EM field only occupies a homogeneous dielectric medium with uniform permittivity and permeability. Thus, our methods also differ from the dielectric approach [20–22].

### **Advantage of superconducting materials**

Longitudinally squeezed cavities have  $V_B$  only limited by penetration depth. Superconductors have a small penetration depth even at very low frequency and enable ultrasmall mode volume. For comparison, superconducting niobium (Nb) has a penetration depth of 40 nm, while the skin depth of copper (Cu) is 2  $\mu\text{m}$  (65  $\mu\text{m}$ ) at 1 GHz (1 MHz).

As  $h$  decreases, a larger fraction of EM energy is in the conductor resulting in ohmic losses. Superconductors mitigate the losses with much smaller surface resistance ( $R_s$ ). Briefly,  $R_s \rightarrow 0$  as  $T \rightarrow 0$  K for BCS superconductors. In practice,  $R_s$  is limited by residual resistances by trapped flux, impurities, or grain boundaries [23]. Overall, Nb has  $R_s = 1 \sim 10$  n $\Omega$  ( $\sim 1$  K,  $\sim 1$  GHz), while Cu

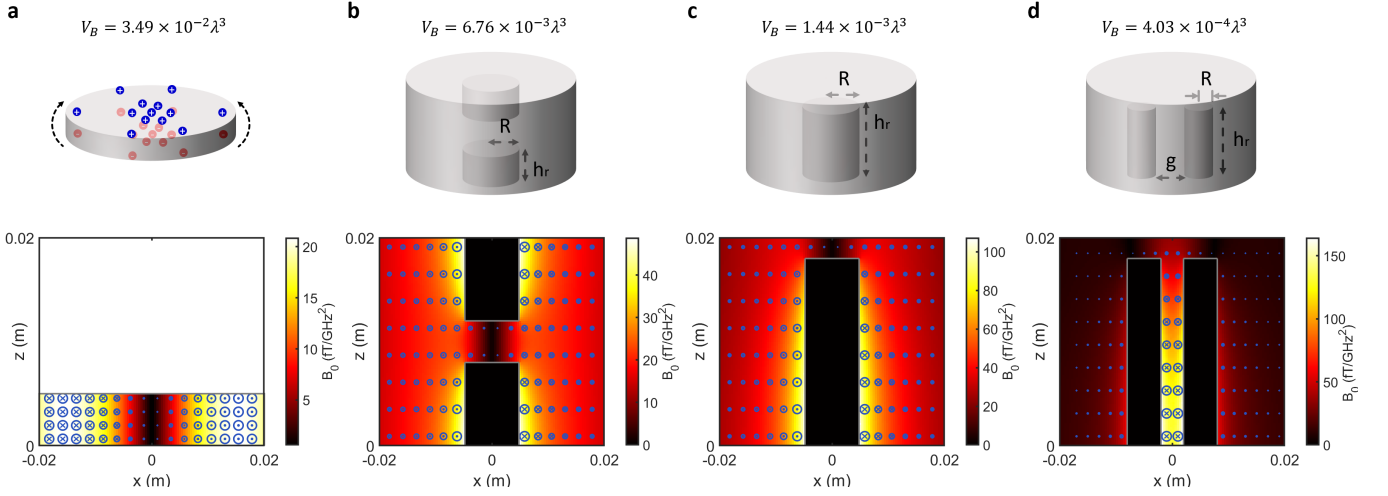


FIG. 2. **Local field enhancement with current engineering.** The colormap represents the norm of the frequency-normalized single-photon magnetic field ( $B_0$ ), and blue circles indicate an out-of-plane magnetic field. The radius of circles is proportional to the magnetic field component in each plot, and  $\bullet$  and  $\circ$  inside the circle represent directions. **a**, Longitudinally squeezed  $TM_{010}$  mode. The blue and red circles illustrate charge densities on top and bottom, and the black arrows show out-of-phase current. **b**, Double split mode cavity ( $R = 5$  mm). **c**, Reentrant cavity ( $R = 5$  mm,  $h_r = 1.8$  cm). **d**, Doubly reentrant cavity ( $R = 3$  mm,  $h_r = 1.8$  cm,  $g = 4$  mm). The currents in the two reentrances are opposing directions. The resonance frequency of each cavity is, **a**,  $f = 5.74$  GHz, **b**,  $f = 3.39$  GHz, **c**,  $f = 2.23$  GHz, and **d**,  $f = 3.21$  GHz.

has  $R_s \sim 1$  m $\Omega$ . Thus, superconductors enable  $10^5 \sim 10^6$  times smaller loss (larger  $Q$ -factor).

### Current engineering

Figure 2a shows the squeezed  $TM_{010}$  mode in the  $xz$ -plane. The mode has a uniformly strong magnetic field around the sidewall. The tangential magnetic field on the conductor is proportional to the surface current, which induces ohmic loss. On the other hand,  $V_B$  strongly depends on the maximum magnetic field in eq. (2), where the dipole is assumed to be.

We consider the cylindrical cavity as an  $LC$  oscillator where the surface charge (current) couples to the electric (magnetic) fields of the  $TM_{010}$  mode;  $\rho_s = \hat{n} \cdot \epsilon_0 \vec{E}$  and  $J_s = \hat{n} \times \vec{H}$ , where  $\rho_s$  and  $J_s$  are the surface charge and current density, and  $\hat{n}$  is the surface normal unit vector. For the  $TM_{010}$  mode, charge oscillates between two parallel plates, and current flows through the side wall  $\pi/2$  out of phase, like the magnetic and electric fields (Fig. 2a).

To strengthen the local magnetic field, we must locally increase the current density. The split-mode cavity in Fig. 2b achieves high current density using two reentrances on the top and bottom [15]. Because the circumference of the reentrances is smaller than the circumference of the cylindrical cavity, the current density is larger on the reentrance surfaces. In addition, the increased capacitance between the top and bottom plates stores more charge resulting in a larger current. Compared to the same height cavity shown in Fig. 1a, the mode volume decreased from  $0.140\lambda^3$  to  $6.76 \times 10^{-3}\lambda^3$ .

The increased  $L$  and  $C$  decrease the resonance frequency from 5.74 GHz to 3.39 GHz. The reentrant cavity [16] or loop-gap cavity [17] can be understood in the same way. Figure 2c shows a reentrant cavity with reentrance radius  $R = 5$  mm and height  $h_r = 1.8$  cm. The cavity has  $V_B = 1.44 \times 10^{-3}\lambda^3$  at  $f = 2.23$  GHz.

On the other hand, a doubly reentrant cavity [18] has two reentrances and a strong magnetic field between them. Figure 2d shows a doubly reentrant cavity with  $R = 3$  mm and the reentrance gap  $g = 4$  mm, further shrinking the mode volume to  $V_B = 4.03 \times 10^{-4}\lambda^3$  at  $f = 3.21$  GHz. One way to understand the cavity mode is by combining the modes of two single-post reentrant cavities, which form symmetric and antisymmetric modes [19]. The antisymmetric mode has a strong magnetic field between the posts induced by two opposite direction currents. Alternatively, the mode can be viewed as a current-engineered  $TM_{110}$  mode. Because it is originated from the  $TM_{110}$  mode, its resonance frequency (3.21 GHz) is higher than that of  $TM_{010}$ -mode derived reentrant cavity (2.23 GHz). (See supplemental for the discussion on the additional mode in a doubly reentrant cavity.)

We show that the current engineering also enables arbitrarily small  $V_B$ . Let's consider a reentrant cavity with vanishingly narrow reentrance, i.e.,  $R \rightarrow 0$ . The capacitance is approximated as that of a cylindrical capacitor,  $C \propto 1/\ln(a/R)$ . The charge, proportional to the capacitance, moves through the reentrance. Applying the integral form of Ampere's law, the magnetic field on the reentrance surface diverges with  $(R \ln(a/R))^{-1}$  scaling

as  $R \rightarrow 0$ . Similarly, the maximum magnetic field of the doubly reentrant cavity diverges as  $\propto (R \ln(g/R))^{-1}$  for  $g \gg R$  and  $\propto 1/g$  for  $R \gg g$  (see Methods).

We can further reduce  $V_B$  using current crowding. In our framework, the capacitance of the reentrance accumulates charge. The charges oscillate through a narrow reentrance producing a strong magnetic field. This design principle thus motivates a large capacitance and narrow conducting channel.

Figure 3 shows the modified reentrant cavity design, where we increased the current density by inverse-tapering the reentrance(s). This inverse tapering combines the benefits of a large capacitance with reentrance top and current crowding. The modified reentrant cavity (Fig. 3a,  $1.76 \times 10^{-5} \lambda^3$ ) has two orders of magnitude smaller  $V_B$  than the non-tapered counterpart (Fig. 2c,  $1.44 \times 10^{-3} \lambda^3$ ). Similarly, the doubly reentrant cavity also shows two orders of magnitude reduction in mode volume from  $4.03 \times 10^{-4} \lambda^3$  (Fig. 2d) to  $5.06 \times 10^{-6} \lambda^3$  (Fig. 3b).

Both designs also achieve arbitrarily small  $V_B$ . Consider a tapered reentrant cavity with fixed top radius  $R$  and variable bottom radius,  $R'$ . When we reduce  $R'$  by more tapering, the capacitance does not decrease significantly as the non-tapered one because the top dominates the capacitance. Thus, the maximum magnetic field of the tapered reentrant cavity scales as  $1/R'$ . Similarly, the magnetic field of a doubly reentrant cavity  $\propto 1/R'$  for  $g \gg R'$  and  $\propto 1/g$  for  $R' \gg g$ . Moreover, the proportionality constant in both cases is larger than the non-tapered ones by increased capacitance.

### Magnetic field expulsion

Lastly, we use magnetic field expulsion for  $V_B$  reduction. The magnetic field expulsion follows from Faraday's law, which shows that good conductors ( $\sigma \gg \omega \epsilon_0$ ) and superconductors expel magnetic field:

$$\vec{\nabla} \times \vec{E} = -j\omega \vec{B} \xrightarrow{\vec{E}=0} \vec{B} = 0. \quad (6)$$

More specifically, the magnetic fields in the quasi-static limit follows,

$$\nabla^2 \vec{B} = \delta^2 \vec{B}, \quad (7)$$

where  $\delta$  is the penetration depth. For superconductors,  $\delta = \lambda_L$  is the London penetration depth (Meissner's effect) and expulsion happens at frequencies below superconducting gap (e.g. Nb: 725 GHz). For normal conductors,  $\delta = (\pi f \sigma \mu)^{-1/2}$  is the skin depth.

Figure 4a shows the magnetic field expulsion of a thin plate in the quasi-static limit. The external magnetic field circumvents the conductor resulting in a stronger magnetic field on the edge. The more elongated the conductor is, the stronger the magnetic field on the edge is. We can express the magnetic field on the surface of a

conductor by the demagnetization factor ( $N$ ) [4, 23–25],

$$B_{\text{surf}} = \frac{B_0}{1 - N}, \quad (8)$$

where  $B_0$  and  $B_{\text{surf}}$  are the external magnetic field and the field at the surface, respectively (see Methods). For an infinitesimally thin conducting plate,  $N \rightarrow 1$ , so that the surface field diverges. Physically, the penetration depth smears out the geometric structure, ending up with a finite field strength.

Figures 4b and 4c show a cavity design after inserting a thin square plate with the length of side  $d = 1.5$  cm and the thickness  $t = 10$   $\mu\text{m}$ , in the cylindrical cavity ( $h = 2$  cm). The gap between the cylindrical wall and the plate is  $g = 2$  mm. With this minimal modification, the mode volume of the cavity reaches  $V_B = 3.18 \times 10^{-5} \lambda^3$ .

Figure 4d shows the mode volume's dependence on the thickness of the inserted plate (blue). We find that  $V_B$  is linearly proportional to the thickness of the plate. An important observation is that  $Q$  does not decrease when reducing  $V_B$  by thinning the plate (Fig. 4d, inset).

We can further reduce the mode volume by increasing  $d$  or decreasing  $g$ . The green markers in Fig. 4d show the mode volume for  $d = 1.9$  cm with the same  $t$  and  $g$ . Similarly, decreasing the gap to  $g = 100$   $\mu\text{m}$  shrink  $V_B$  (red). From the inset, We find that these modifications also reduce  $Q$ . However, for all cases, decreasing  $t$  does not degrade  $Q$ .

### Cavity comparison

We first define a material independent metric for the loss of a cavity. The geometric factor of a cavity is

$$G = \frac{\omega \mu_0 \int |\vec{B}|^2 dV}{\int |\vec{B}|^2 dS}. \quad (9)$$

We can express quality factors of a hollow metallic cavity with  $G$  and surface resistance ( $R_s$ ) of the metal;

$$Q = \frac{G}{R_s}. \quad (10)$$

Figure 5 summarizes the trade-off between  $G$  and  $V_B$  for the cavity designs. The right  $y$ -axis shows the expected  $Q$  for Nb (Cu) cavity with  $R_s = 10$  n $\Omega$  (1 m $\Omega$ ). Each color represents different cavity designs with illustration. We fixed  $h$  for all designs except the cylindrical cavity design. The minimum feature size of reentrances is 100  $\mu\text{m}$ , and the minimum thickness of plates is 10  $\mu\text{m}$ . The magnetic field for  $V_B$  calculation is probed 50  $\mu\text{m}$  away from reentrances or 5  $\mu\text{m}$  away from the edge of the plate considering emitter placement. We emphasize that the markers and shades are representative, but not limiting accessible  $Q$  and  $V_B$ . Higher  $Q$  or smaller  $V_B$  are in principle possible with more aggressive assumptions on the cavity fabrication or operation frequencies.

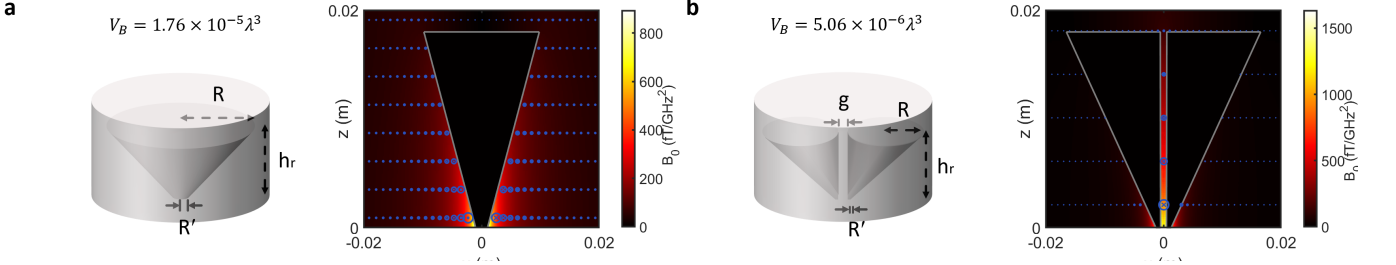


FIG. 3. **Inverse-tapered reentrances for current crowding.** **a**, A tapered reentrant cavity ( $f = 1.41$  GHz). The radius of the reentrance top and bottom are  $R = 1$  cm and  $R' = 1$  mm, respectively. Reentrance height is  $h_r = 1.8$  cm. **b**, A tapered doubly reentrant cavity ( $f = 2.12$  GHz).  $R = 8$  mm,  $R' = 0.8$  mm,  $h_r = 1.8$  cm, and the gap between two reentrances is  $g = 2$  mm.

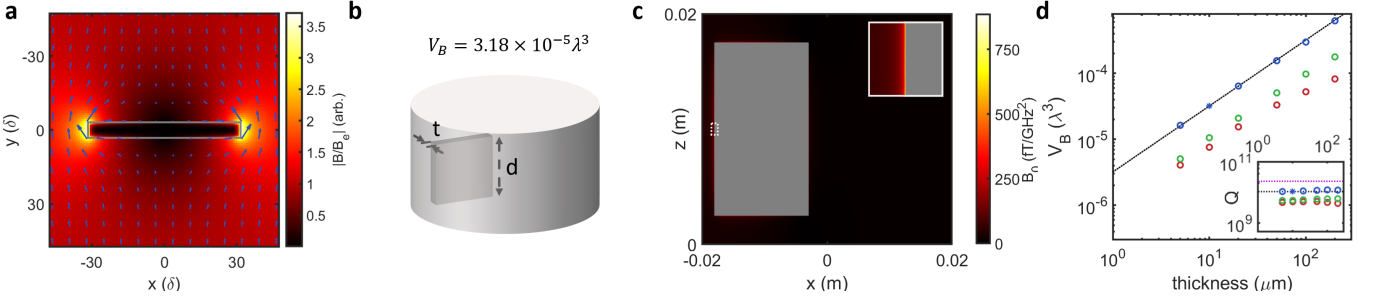


FIG. 4. **Magnetic field expulsion.** **a**, Magnetic field expulsion by a thin metallic plate. The field distribution is calculated assuming the quasi-static limit, where the size of the plate is much smaller than the wavelength of the external field ( $B_e$ ). Magnetic field near the edge of the plate is enhanced compared to the uniform magnetic field applied. **b**, A cylindrical cavity with a thin plate of metal. **c**, The magnetic field distribution of  $TM_{010}$ -like mode. (Inset) close-up view of dotted rectangle region. **d**,  $V_B$  vs. thickness of the plate. (blue)  $d = 1.5$  cm,  $g = 2$  mm, (green)  $d = 1.9$  cm,  $g = 2$  mm, (red)  $d = 1.5$  cm,  $g = 100$   $\mu$ m. The blue asterisk represents the cavity in **c**. (dotted line)  $V_B/\lambda^3 = (3.2 \mu m^{-1}) \cdot t$ .  $r_e^-$  is chosen for maximum  $B(r_e^-)$  restricted with half the thickness away from the plate. The inset shows  $Q$  for the cavities.  $Q$  changes negligibly on  $t$ . As a reference,  $Q$  of the plain cylindrical cavity is marked with a purple dashed line.

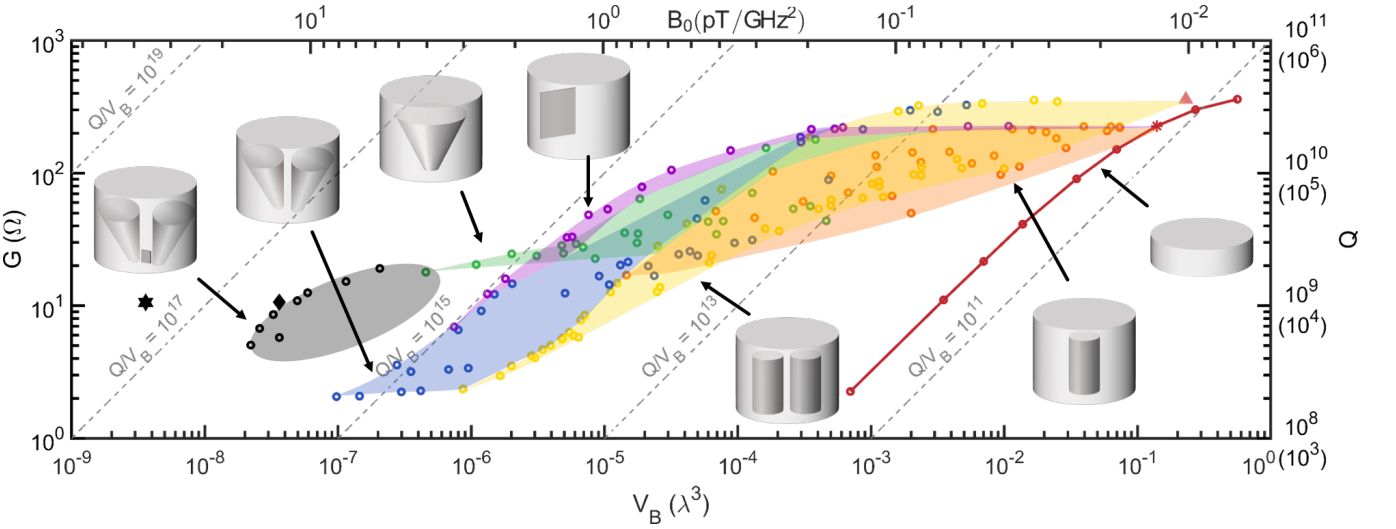


FIG. 5. **Geometric factors (quality factors) vs. mode volumes (single photon magnetic fields).**  $Q$  (right axis) is calculated assuming a Nb superconducting cavity with  $R_s = 10$  m $\Omega$ . The values in the parenthesis is for Cu cavity ( $R_s = 1$  m $\Omega$ ). The mode volume (bottom axis) is normalized to the diffraction-limited volume ( $\lambda^3$ ). Each color of markers represent different cavity designs as illustrated. Each marker is the simulated value of different cavity dimension parameters, and the shaded region is the trade-off space the design can access with the fabrication assumptions. The markers and shades are representative (see main text).

The red circles show the simulated value of cylindrical cavities. As the  $h$  decreases,  $V_B$  proportionally decreases. A longitudinally squeezed cavity with  $h = 100 \mu\text{m}$  reaches  $V_B = 7.00 \times 10^{-4} \lambda^3$ . On the other hand,  $Q$  is nearly unchanged for  $h \gg r$  because the side wall dominates the loss, but  $Q$  decreases proportionally for  $h \ll r$  by the dominant loss from the top and bottom plates. Thus, the longitudinal squeezing for  $h \ll r$  decreases both  $V_B$  and  $Q$ , with  $Q/V_B \sim 3 \times 10^{11} \lambda^{-3}$  (Nb) unchanged.

Current engineered cavities achieve not only smaller  $V_B$  but also higher  $Q/V_B$ . Starting from the  $h = 2 \text{ cm}$  cylindrical cavity (red asterisk), we introduce a reentrance (orange). For a thin and short reentrance,  $Q$  barely changes with reduced  $V_B$ . However, to further reduce the mode volume, given the minimum radius  $R = 100 \mu\text{m}$ , we need taller reentrances to increase the capacitance. When the sidewalls dominate the loss (small  $h_r$ ), increasing  $h_r$  does not decrease  $Q$ . When the reentrance dominates the loss (large  $h_r$ ), increasing  $h_r$  decreases  $V_B$  with marginal  $Q/V_B$  improvement.

Doubly reentrant cavities (yellow circles) also have a  $V_B$ - $Q$  trade-off, starting from the  $\text{TM}_{110}$  mode (pink triangle). The smallest  $V_B \approx 8.68 \times 10^{-7}$  is an order of magnitude smaller than that of reentrant cavities ( $V_B \approx 1.46 \times 10^{-5}$ ). The inverse-tapered reentrant (green circles) and doubly reentrant cavities (blue circles) have similar behavior but with an additional order of magnitude smaller  $V_B = 4.56 \times 10^{-7} \lambda^3$  and  $V_B = 9.39 \times 10^{-8} \lambda^3$ , respectively. The inverse-tapered cavities include the trade-off space of non-tapered cavities, we did not include for the visibility.

The field expulsion cavities (purple circles) can reach  $V_B = 3.57 \times 10^{-4} \lambda^3$  with negligible reduction in  $Q$ . The flat  $V - Q$  trade-off is obtained by thinning the inserted plate. Further reduction of  $V_B$  is possible with either increasing  $d$  or decreasing  $g$ , and the minimum  $V_B = 7.45 \times 10^{-7} \lambda^3$ .

Lastly, we present a cavity design combining the current engineering and field expulsion. In the design, we inserted a thin plate into the inverse-tapered doubly reentrant cavity (black circles). The highest  $Q/V_B$  approaches  $3 \times 10^{16} \lambda^{-3}$  (black diamond), which is five orders of magnitude larger than the bare cylindrical cavity. If the plate in the design is thinned down to  $1 \mu\text{m}$ , the mode volume will reach  $V_B = 3.6 \times 10^{-9} \lambda^3$  (black star).

We also emphasize that the mode volume in units of  $\lambda^3$ , for a given minimum feature size, can be much smaller at lower operation frequencies. In this analysis, we consider  $f = 1 \sim 10 \text{ GHz}$  for the applications below, but by operating at  $f \approx 10 \text{ MHz}$ , one could easily achieve  $V_B < 10^{-11} \lambda^3$  and  $Q/V_B > 10^{20} \lambda^{-3}$  with minimum feature size of  $100 \mu\text{m}$  and plate thickness of  $1 \mu\text{m}$ . Note that  $Q/V_B = 10^{20} \lambda^{-3}$  corresponds to Purcell enhancing an emitter decaying slower than the age of the universe, to decay within a few tens of milliseconds.

## Discussion

Extreme values of  $Q/V_B$  with our cavity designs open up new possibilities in the control of magnetic light-matter interactions, including in (i) microwave photon-spin coupling, (ii) magnetic circuit QED, (iii) ultraprecision metrology [26], (iv) dark-matter searches [27, 28], etc. We elaborate briefly on the first two examples.

(i) Solid-state spin qubits such as nitrogen vacancy centers have demonstrated coherence time ( $T_2^*$ ) of  $1.5 \text{ ms}$  [29]. Coupling a single NV center to the cavity indicated in Fig. 5 as the black diamond, at  $10 \text{ GHz}$ , would show a high cooperativity  $C = 4g^2/\kappa\gamma^* = 12.5$ , where  $g$  is the coupling rate,  $\kappa$  is the cavity dissipation rate, and  $\gamma^*$  is the dephasing rate. The interaction can be greatly increased with spin ensembles or magnons by the number of spins;  $C = 4Ng^2/\kappa\Gamma$  where  $N$  is the number of spins, and  $\Gamma$  is the ensemble dephasing rate. However, the single-spin operation enables a full quantum nonlinearity with a wide range of applications including MW-optical transduction [30] for quantum networks and thresholdless [31], single-spin [32] ultralow-noise masers [33]. The number of spins in our calculation is twelve orders of magnitude smaller than the early efforts [9, 18, 34] and six orders of magnitude smaller than the recent state-of-the-art with the lumped-element/3D hybrid approach  $\sim 1.5 \times 10^6$  [35].

(ii) On the other hand, the flux qubit family (RF-SQUID, 3-junction flux qubit, fluxonium) can be coupled to the cavity.  $6 \mu\text{m} \times 5 \mu\text{m}$  loop used in [36] magnetically can couple with the cavity with  $g \sim 2.33 \text{ MHz}$  at  $5 \text{ GHz}$ , achieving a strong coupling regime. In addition, the qubit will be located at the magnetic field antinode, where the electric field is minimal, potentially introducing negligible cavity loss from two-level systems in substrate dielectrics.

## Conclusion

In conclusion, we described design methods to shrink the magnetic mode volume of electromagnetic cavities. The resulting mode volume of all three methods can be arbitrarily small, only limited by the material's penetration depth or practically the fabrication resolution. We benchmarked different cavity designs in terms of mode volume and loss. The geometric factor, a material-independent metric for loss, only decreases ten times for more than a million times smaller mode volume (black diamond in Fig. 5). This corresponds to  $Q = 1.06 \times 10^9$  with  $V_B = 3.62 \times 10^{-8} \lambda^3$  for superconducting niobium. This opens the possibilities of quantum applications such as cavity quantum magneto-dynamics (cQMD) with spins or superconducting artificial atoms, and magnetic nonlinear devices.

Future work should modify the designs for fabrication ease, operational frequency, or multimode operation (see some examples in the Supplemental). Depending on the application, the figures of merit would be  $1/V_B$  (Purcell

effect in BE),  $1/\sqrt{V_B}$  (vacuum Rabi-splitting in BE), or  $Q/\sqrt{V_B}$  (vacuum Rabi-splitting in BC) [20], where BE and BC stands for bad emitter and bad cavity regime. Nonlinear (magnetic) optical applications benefit from high magnetic field over the volume of nonlinear medium with the figure of merit  $Q^2/V_{\text{Kerr}}$  (nonlinear bistability) or  $QV_M/V_B^2$  (Kerr blockade) [20]. Moreover, cascaded cavities coupled with quantum emitters have richer dynamics with advantages over the single cavity system [22]. Furthermore, certain applications will benefit from other materials, such as high- $T_c$  superconductors for liquid nitrogen temperature operations.

---

\* choihr@mit.edu

† englund@mit.edu

- [1] L. M. Vandersypen and I. L. Chuang, *Rev. Mod. Phys.* **76**, 1037 (2005).
- [2] N. Crescini, C. Braggio, G. Carugno, A. Ortolan, and G. Ruoso, *Appl. Phys. Lett.* **117**, 144001 (2020).
- [3] N. Bloembergen, E. M. Purcell, and R. V. Pound, *Phys. Rev.* **73**, 679 (1948).
- [4] D. M. Pozar, *Microwave engineering* (John Wiley & sons, 2011).
- [5] M. Oxborrow, J. D. Breeze, and N. M. Alford, *Nature* **488**, 353 (2012).
- [6] L. Novotny and B. Hecht, *Principles of nano-optics* (Cambridge university press, 2012).
- [7] A. Wallraff, D. I. Schuster, A. Blais, L. Frunzio, R.-S. Huang, J. Majer, S. Kumar, S. M. Girvin, and R. J. Schoelkopf, *Nature* **431**, 162 (2004).
- [8] P. Krantz, M. Kjaergaard, F. Yan, T. P. Orlando, S. Gustavsson, and W. D. Oliver, *Appl. Phys. Lett.* **6**, 021318 (2019).
- [9] Y. Kubo, F. Ong, P. Bertet, D. Vion, V. Jacques, D. Zheng, A. Dréau, J.-F. Roch, A. Auffèves, F. Jelezko, *et al.*, *Phys. Rev. Lett.* **105**, 140502 (2010).
- [10] Y. Kubo, C. Grezes, A. Dewes, T. Umeda, J. Isoya, H. Sumiya, N. Morishita, H. Abe, S. Onoda, T. Ohshima, *et al.*, *Phys. Rev. Lett.* **107**, 220501 (2011).
- [11] Y. Kubo, I. Diniz, C. Grezes, T. Umeda, J. Isoya, H. Sumiya, T. Yamamoto, H. Abe, S. Onoda, T. Ohshima, *et al.*, *Phys. Rev. B* **86**, 064514 (2012).
- [12] J. M. Sage, V. Bolkhovskiy, W. D. Oliver, B. Turek, and P. B. Welander, *J. Appl. Phys.* **109**, 063915 (2011).
- [13] H. Paik, D. Schuster, L. S. Bishop, G. Kirchmair, G. Catelani, A. Sears, B. Johnson, M. Reagor, L. Frunzio, L. Glazman, *et al.*, *Phys. Rev. Lett.* **107**, 240501 (2011).
- [14] P. Campagne-Ibarcq, A. Eickbusch, S. Touzard, E. Zalys-Geller, N. E. Frattini, V. V. Sivak, P. Reinhold, S. Puri, S. Shankar, R. J. Schoelkopf, *et al.*, *Nature* **584**, 368 (2020).
- [15] J.-M. Le Floch, N. Delhote, M. Aubourg, V. Mdrangeas, D. Cros, S. Castelletto, and M. Tobar, *J. Appl. Phys.* **119**, 153901 (2016).
- [16] R. G. Carter, J. Feng, and U. Becker, *IEEE Trans. Microw. Theory Tech.* **55**, 2531 (2007).
- [17] D. K. Park, G. Feng, R. Rahimi, J. Baugh, and R. Laflamme, *J. Magn. Reson.* **267**, 68 (2016).
- [18] D. L. Creedon, J.-M. Le Floch, M. Goryachev, W. G. Farr, S. Castelletto, and M. E. Tobar, *Phys. Rev. B* **91**, 140408 (2015).
- [19] M. Goryachev, W. G. Farr, D. L. Creedon, Y. Fan, M. Kostylev, and M. E. Tobar, *Phys. Rev. Appl.* **2**, 054002 (2014).
- [20] H. Choi, M. Heuck, and D. Englund, *Phys. Rev. Lett.* **118**, 223605 (2017).
- [21] S. Hu and S. M. Weiss, *ACS Photonics* **3**, 1647 (2016).
- [22] H. Choi, D. Zhu, Y. Yoon, and D. Englund, *Phys. Rev. Lett.* **122**, 183602 (2019).
- [23] M. Tinkham, *Introduction to superconductivity* (Courier Corporation, 2004).
- [24] J. D. Jackson, *Classical electrodynamics* (John Wiley & Sons, 2007).
- [25] J. Osborn, *Phys. Rev.* **67**, 351 (1945).
- [26] J. Ye, H. Kimble, and H. Katori, *science* **320**, 1734 (2008).
- [27] Y. Kahn, B. R. Safdi, and J. Thaler, *Physical review letters* **117**, 141801 (2016).
- [28] A. Garcon, J. W. Blanchard, G. P. Centers, N. L. Figueroa, P. W. Graham, D. F. J. Kimball, S. Rajendran, A. O. Sushkov, Y. V. Stadnik, A. Wickenbrock, *et al.*, *Science advances* **5**, eaax4539 (2019).
- [29] E. Herbschleb, H. Kato, Y. Maruyama, T. Danjo, T. Makino, S. Yamasaki, I. Ohki, K. Hayashi, H. Morishita, M. Fujiwara, *et al.*, *Nat. Commun.* **10**, 1 (2019).
- [30] J. G. Bartholomew, J. Rochman, T. Xie, J. M. Kindem, A. Ruskuc, I. Craiciu, M. Lei, and A. Faraon, *Nat. Commun.* **11**, 1 (2020).
- [31] T. Kobayashi, T. Segawa, Y. Morimoto, and T. Sueta, in *46th Fall Meeting of the Japanese Applied Physics Society* (1982).
- [32] J. McKeever, A. Boca, A. D. Boozer, J. R. Buck, and H. J. Kimble, *Nature* **425**, 268 (2003).
- [33] J. D. Breeze, E. Salvadori, J. Sathian, N. M. Alford, and C. W. Kay, *Nature* **555**, 493 (2018).
- [34] D. Schuster, A. Sears, E. Ginossar, L. DiCarlo, L. Frunzio, J. Morton, H. Wu, G. Briggs, B. Buckley, D. Awschalom, *et al.*, *Phys. Rev. Lett.* **105**, 140501 (2010).
- [35] A. Bienfait, *Magnetic resonance with quantum microwaves*, Ph.D. thesis, Université Paris-Saclay (2016).
- [36] F. Yan, S. Gustavsson, A. Kamal, J. Birenbaum, A. P. Sears, D. Hover, T. J. Gudmundsen, D. Rosenberg, G. Samach, S. Weber, *et al.*, *Nat. Commun.* **7**, 1 (2016).



## Methods

**Numerical simulation of cavities.** All numerical results are obtained using finite element method (FEM) with a commercial software (COMSOL). We used tetrahedral meshes with the maximum  $1 \sim 2$  mm. The minimum mesh size is chosen to be less than half the minimum feature size (e.g., thickness of the plate in Fig. 4c). The maximum element growth rate is set to  $1.35 \sim 1.45$  with curvature factor of  $\sim 0.4$  and narrow region resolution of  $\sim 0.7$ .

**TM<sub>010</sub> mode volume.**

$$\int dV B^2 / \mu_0 = \int dV \epsilon_0 E^2 \quad (11)$$

$$= 2\pi h \epsilon_0 |E_0|^2 \int_0^a r |J_0(j_{01} r/a)|^2 dr \quad (12)$$

$$= 2\pi h \cdot a^2 \cdot \epsilon_0 |E_0|^2 \int_0^1 x |J_0(j_{01} x)|^2 dx \quad (13)$$

$$\approx 0.135 \cdot 2\pi h \cdot a^2 \epsilon_0 |E_0|^2. \quad (14)$$

$$V_B = (0.135 \cdot 2\pi h \cdot a^2) \cdot \left(\frac{a}{j_{01}}\right)^2 \cdot \frac{\omega^2 \mu_0 \epsilon_0}{|J'_0(j_{\max})|^2} \quad (15)$$

$$\approx \frac{0.135}{0.339} \cdot 2\pi h \cdot \left(\frac{j_{01}}{k}\right)^2 \quad (16)$$

$$\approx 0.0635 \cdot |j_{01}|^2 \cdot h \cdot \lambda^2 \quad (17)$$

$$\approx 0.366 \cdot h \cdot \lambda^2 \quad (18)$$

where  $j_{\max} \in [0, j_{01})$  maximizes  $|J'_0(j_{\max})|^2$ .

**$V_B$  scaling of doubly reentrant cavities.** The capacitance of two-wire transmission line (per unit length) is  $C = \pi \epsilon_0 / \cosh^{-1}((g+2R)/2R) \approx \pi \epsilon_0 / \ln(g/R)$  for  $g \gg R$ . The currents proportional to the capacitance uniformly distribute over the circumference of the reentrance in this limit. Thus, the maximum magnetic field scales as  $(R \ln(g/R))^{-1}$ . For  $g \ll R$ ,  $C \approx \pi \epsilon_0 \cdot \sqrt{R/g}$ . Current proportional to the capacitance creates a flux proportional to the inductance  $L \approx \pi \mu_0 \cdot \sqrt{g/R}$ . Scaling of  $L$  and  $C$  cancels each other, and magnetic field scales as  $1/g$  assuming it is uniform across the gap.

**The demagnetization factor.** The relation between  $B_{\text{surf}}$  and  $N$  shown in Eq. (8) needs a specification on  $N$ . An ellipsoid in a uniform magnetic field has uniform demagnetization field [24], and  $N$  can be unequivocally defined;  $N = 1 - E(\sqrt{1 - b^2/a^2}) \cdot c/b$ , where  $a \geq b \gg c$  are half the length of principal axes, and  $E$  is the complete elliptic integral of the second kind. (See [25] for the full analytic expression in general cases.) We find as  $a = b$  and  $c/b \rightarrow 0$ , that  $N \approx 1 - c/b$  and  $B_{\text{surf}} \approx b/c \rightarrow \infty$ . We can extend Eq. (8) to non-ellipsoidal cases by defining an effective demagnetization factor  $N_{\text{eff}} = 1 - B_0/B_{\text{surf}}$ . It can be easily shown that an infinitesimally thin superconducting plate with  $\lambda_L \rightarrow 0$  has  $N_{\text{eff}} \rightarrow 1$  from the magnetic Poisson's equation [24].

**Coupling rate calculation.** For solid-state spin qubits, we used the gyromagnetic ratio of electronic spin  $\gamma = 28$  GHz/T. At 10 GHz,  $V_B = 3.62 \times 10^{-8} \lambda^3$  corresponds to  $B_s = 2.06$  nT and  $g = 57.7$  Hz.

For a superconducting flux qubit, we calculate the magnetic transition dipole moment,  $m_0$ . Near the sweet spot, the computational basis of a flux qubit is a symmetric and antisymmetric combination of clockwise and anticlockwise circulating current (equivalent to  $n$  and  $n+1$  flux quantum in the superconducting loop):  $|0\rangle = \sqrt{1/2}(|\circ\rangle + |\oslash\rangle)$  and  $|1\rangle = \sqrt{1/2}(|\circ\rangle - |\oslash\rangle)$ . The transition dipole moment is,

$$\begin{aligned} m_0 = \langle 0 | \hat{m} | 1 \rangle &= \frac{1}{2} (\langle \circ | \hat{m} | \circ \rangle - \langle \oslash | \hat{m} | \oslash \rangle) \\ &= A \cdot \langle \circ | \hat{I} | \circ \rangle, \end{aligned} \quad (19)$$

where  $\hat{I}$  is the current operator, and  $A$  is the area of a superconducting loop. Assuming a  $6 \mu\text{m} \times 5 \mu\text{m}$  loop and circulating current  $\langle \circ | \hat{I} | \circ \rangle = 100$  nA, used in [36],  $m_0 = 3 \mu\text{A} \cdot \mu\text{m}^2$ . Thus,  $g = B_s \cdot m_0 / h = 2.33$  MHz at  $f = 5$  GHz ( $B_s$  of the cavity marked as the black diamond in Fig. 5.)

## Data availability

The data that support the plots within this paper and other findings of this study are available from the corresponding authors upon reasonable request.

## Acknowledgement

We thank Kevin O'Brien, Karl Berggren, Qing Hu, William D. Oliver, Youngkyu Sung, Don Fahey, Jonathan Hoffman, Daniel Freeman, Shantanu Rajesh Jha, Max Hays, Shoumik Chowdhury, and Kyle Serniak for fruitful discussion. This work was supported in part by the Defense Advanced Research Projects Agency (DARPA) DRINQS (HR001118S0024) program. H.C acknowledges the Claude E. Shannon Fellowship and the Samsung Scholarship.

## Author Contributions

H.C. conceived and simulated the design methods. H.C. and D.E. analyzed and discussed the results. H.C. wrote the manuscript with the assistance of D.E.

## Competing interests

Authors declare no conflicts of interest.

## Additional information

Supplementary information is available for this paper.